
Article:
Wang, D. orcid.org/0000-0001-6957-2494, Zhang, S., Wang, G. et al. (6 more authors) (2020) Cold sintered CaTiO3-K2MoO4 microwave dielectric ceramics for integrated microstrip patch antennas. Applied Materials Today, 18. 100519. ISSN 2352-9407

https://doi.org/10.1016/j.apmt.2019.100519

Cold Sintered $CaTiO_3$-K_2MoO_4 Microwave Dielectric Ceramics for Integrated Microstrip Patch Antennas

Dawei Wang[a#*], Shiyu Zhang[b#], Ge Wang[a], Yiannis Vardaxoglou[b], Will Whittow[b], Darren Cadman[b], Di Zhou[c], Kaixin Song[a,d], Ian M Reaney[a*]

[a]*Department of Materials Science and Engineering, University of Sheffield, Sheffield S1 3JD, UK*

[b]*Wolfson School of Mechanical, Electrical and Manufacturing Engineering, Loughborough University, Loughborough LE11 3TU, UK*

[c]*Electronic Materials Research Laboratory, Key Laboratory of the Ministry of Education & International Center for Dielectric Research, Xi'an Jiaotong University, Xi'an 710049, Shaanxi, China*

[d]*College of Electronics Information, Hangzhou Dianzi University, Hangzhou 310018, China*

* Corresponding author. E-mail address: dawei.wang@sheffield.ac.uk, i.m.reaney@sheffield.ac.uk

[#] Author Contributions: D. Wang and S. Zhang contributed equally to this work.

ABSTRACT

$CaTiO_3$-K_2MoO_4 (CTO-KMO) dielectric composites were successfully cold-sintered at 150 °C for 30 min with a uniaxial pressure of 200 MPa. X-ray diffraction, Raman spectroscopy, back-scattered SEM and energy dispersive x-ray mapping confirmed the coexistence of CTO and KMO with no evidence of interdiffusion and parasitic phases either between the two ceramic end-members or with Ag internal electrodes. As KMO concentration increased, the temperature coefficient of resonant frequency (TCF) and relative pemittivity (ε_r) decreased but the microwave quality factor ($Q\times f$) increased. A near-zero TCF composition was obtained for CTO-0.92KMO composites which exhibited ε_r ~ 8.5 and $Q\times f$ ~ 11,000 GHz. A microstrip patch antenna was designed and fabricated using cold sintered CTO-0.92KMO as a substrate (40×40×1.4 mm), which gave a s11 of -14.2 dB and a radiation efficiency of 62.0% at 2.51 GHz.

KEYWORDS: cold sintering, microwave dielectric ceramics, microstrip patch antenna

INTRODUCTION

Fifth generation (5G) cellular network technology provides far faster and more reliable broadband access, with greater capacity and lower response times. New microwave (MW) materials are however, required to maximise the use of frequency ranges that have been made available for 5G. 5G requires components with lower power consumption (dielectric loss < 0.001), shorter delay times (latency, t_{pd} <1 ms as opposed to < 25 ms) and greater functionality than their 4G counterparts.[1-5] Latency depends on the relative permittivity (ε_r) of ceramics, according to:

$$t_{pd} = \frac{\ell\sqrt{\varepsilon_r}}{c}, \quad (1)$$

where ℓ = transmission distance, c = speed of light in vacuum. Therefore, antennas, resonators, filters, substrates and microstrip lines in 5G communication devices will require low dielectric loss, low ε_r (<15) materials, such as alumina, silicates, molybdates, borates and tungstates.[6-14] However, ceramics are manufactured using conventional sintering technology (>1000 ºC) and thus cannot be directly integrated into polymer circuit boards (PCBs). Therefore, to truly create a revolution in RF component manufacture for 5G technology, integrated ceramic components are required which densify at temperatures less than that of the melting point of polymers (typically < 200°C). Until recently, this was considered impossible but cold sintering, emerging from the group of Randall and co-workers is capable of densifying MW ceramics and composites at < 200°C, including Li_2MoO_4 (LMO), MoO_3, $Na_2Mo_2O_7$ (NMO), $K_2Mo_2O_7$, $(LiBi)_{0.5}MoO_4$, LMO-PTFE, Al_2SiO_5-NaCl, and LMO-$BaFe_{12}O_{19}$.[15-30] Recent work has demonstrated that low temperature coefficient of resonant frequency (TCF) (<+/-10 ppm/°C) and ε_r ($17 < \varepsilon_r < 50$) is achieved in cold-sintered LMO-$Na_{0.5}Bi_{0.5}MoO_4$ and NMO $(Bi_{0.95}Li_{0.05})(V_{0.9}Mo_{0.1})O_4$ dielectric composite ceramics[31-33] but, to date, no reported cold-sintered MW material with near-zero TCF meet the requirements of 5G technology, i.e. low ε_r and low dielectric loss (tanδ, high quality factor $Q\times f$). In the present work, end-members, $CaTiO_3$ (CTO, ε_r = 160, TCF = +850 ppm/°C)[34]

and K_2MoO_4 (KMO, ε_r = 6.37, TCF = -70 ppm/°C)[32], were selected to prepare a series of ceramic composites with the prospect for producing a low ε_r (<15), near-zero TCF and high $Q \times f$ material suitable for 5G antenna substrates.

EXPERIMENTAL SECTION

To prepare (1-x)CTO-xKMO (x = 0.2, 0.5, 0.7, 0.8, 0.92, 1 in weight) composite ceramics, commercial CTO (Alfa Aesar, > 99%) and KMO (Alfa Aesar, > 95%) powder were mixed with a small amount of deionized water (5-10 wt%). The mixtures were hot-pressed 30 min at 150 °C and 200 MPa and dried 24 h at 120 °C to remove any remaining moisture. The bulk density of sintered pellets was calculated by a geometric method. The microstructure, crystal structure and phase assemblage was revealed by FEI Inspect F-50 scanning electron microscopy (SEM), Bruker D2 Phaser X-ray powder diffraction (XRD) and Renishaw inVia Raman spectroscopy, respectively. The $TE_{01\delta}$ dielectric resonator method was used to measure ε_r, TCF, tanδ and $Q \times f$, in conjunction with an Advantest R3767CH vector network analyzer (Tokyo, Japan). To determine TCF, the resonant frequency (f) was measured in a heated cavity by a Peltier device in a temperature range of 25 °C ~ 85 °C, and then inputted into Equation (2).

$$\mathrm{TCF} = \frac{f_T - f_{T_0}}{f_{T_0} \times (T - T_0)} \times 10^6 \quad (2)$$

where the f_T and f_{T_0} were f at temperatures of T and T_0, respectively.

RESULTS AND DISCUSSION

Relative densities (ρ_r) of cold-sintered CTO-xKMO ceramic composites are listed in Table 1, which increased from 89% for CTO-0.2KMO to 100% for compositions with x > 0.5.

Table I. Relative densities (ρ_r), and microwave dielectric properties of CTO-KMO ceramics.

Composition	ρ_r (%)	ε_r	$tan\delta$	$Q\times f$ (GHz)	TCF (ppm/^{o}C)
CTO-0.2KMO	89	46.6	0.004	1000	+317
CTO-0.5KMO	97	37.2	0.004	1030	+274
CTO-0.7KMO	100	20.9	0.001	4360	+142
CTO-0.8KMO	100	13.7	0.0008	7170	+70
CTO-0.92KMO	100	8.5	0.0008	11000	-4
KMO	100	6.4	0.0003	26470	-70

Room-temperature XRD patterns and Raman spectra of commercial CTO powder and cold-sintered CTO-xKMO samples are shown in Fig. 1. CTO and KMO exhibit a perovskite orthorhombic (space group: *Pnma*, PDF card: 42-423) and a monoclinic structure (space group: *C12/m1*, PDF card: 29-1021), respectively. All diffraction peaks in the XRD patterns for CTO-xKMO are assigned to either CTO and KMO and the reflection intensities of KMO increase with increasing weight fraction, as labelled in Fig. 1(a). Coexistence of diffraction peaks related to CTO and KMO is found in all studied composites with $0 < x < 1$, with no trace of impurity peaks or shift of peak positions, indicating that there is no detectable interaction between CTO and KMO. To confirm the weight fraction of each end member in the composites, full-pattern Rietveld refinement of X-ray data was conducted using a two phase mix of CTO (*Pnma*) and KMO (*C12/m1)* with CTO-0.2KMO and CTO-0.8KMO given in Fig. 1(c) and (d), respectively. Good agreement is observed between the experimental and calculated patterns with weight fractions close to the nominal compositions.

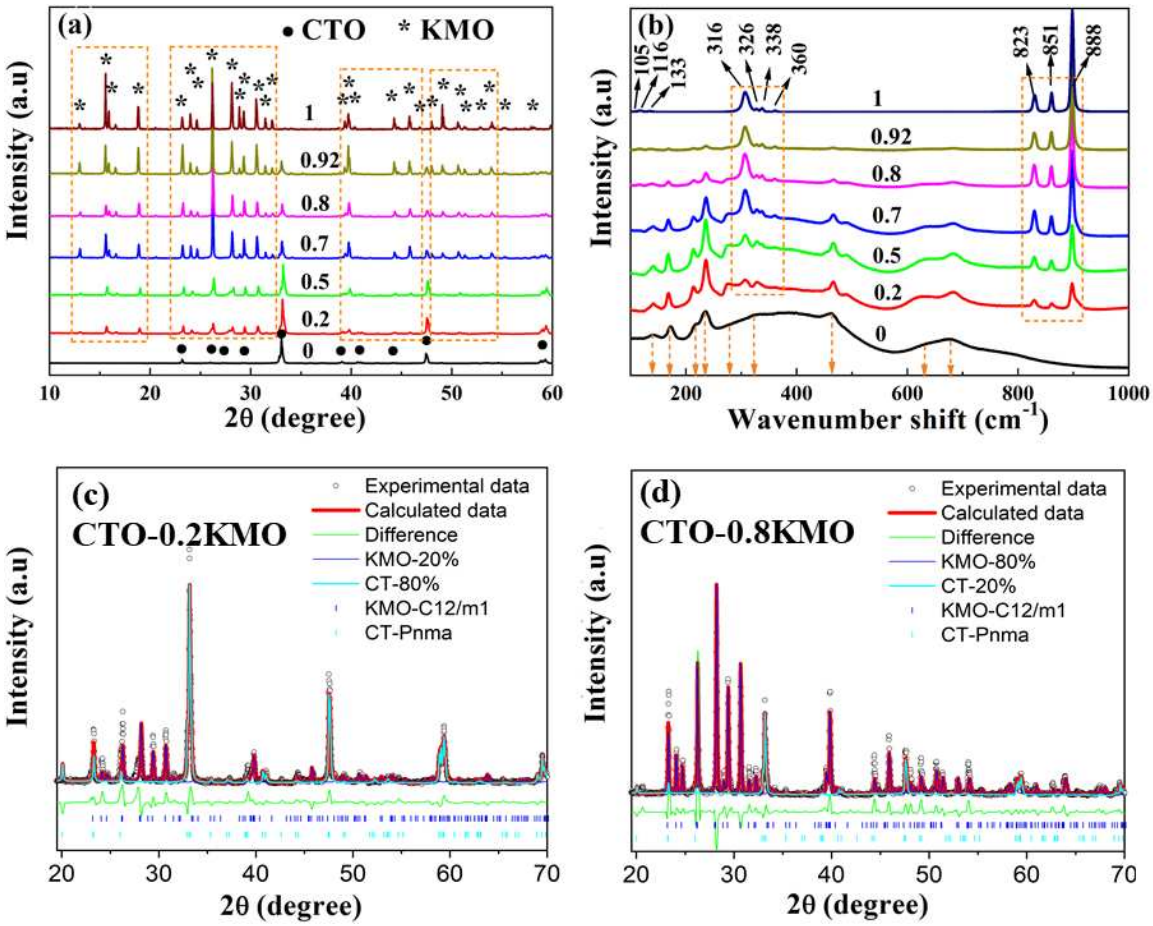

Figure 1. Room-temperature (a) XRD patterns and (b) Raman spectra of CTO-xKMO composite ceramics.

For orthorhombic (*Pnma*) CTO, a total of 117 vibrational modes are expected (24 Raman-active modes) according to previous reports.[35-37] However, most of these bands cannot be observed due to their low change in polarizability. Instead, ten main Raman bands are observed for CTO at 140, 172, 220, 235, 275, 323, 463, 492, 630 and 678 cm^{-1}, which are assigned to the Ti–O symmetric stretching (630, 678 cm^{-1}), Ti–O torsional mode (bending or internal vibration of oxygen cage, 463, 492 cm^{-1}), O-Ti–O bending (172, 220, 235, 275, 323 cm^{-1}) and motion of A-site ions (140 cm^{-1}). Based on the group theory together with irreducible representations, 39 vibrational modes are found in KMO,[38-39] given as follows:

$$\Gamma_{KMO} = 13A_g + 7A_u + 8B_g + 11B_u \quad (3)$$

18 modes of $6A_g + 3A_u + 3B_g + 6B_u$ are assigned to the internal modes of MoO_4 tetrahedra, where the stretching modes are distributed as $2\nu_1$ (A_g+B_u) and $6\nu_3$ ($2A_g+A_u+B_g+2B_u$) and the bending modes are distributed as follows $4\nu_2$ ($A_g+A_u+B_g+B_u$) and $6\nu_4$ ($2A_g+A_u+B_g+2B_u$). The remaining lattice modes are related to the translations of the potassium ions ($4A_g+2A_u+2B_g+4B_u$), vibrations of the MoO_4 tetrahedra ($A_g+2A_u+2B_g+B_u$) and translations of the MoO_4 tetrahedra ($2A_g+A_u+B_g+2B_g$). Only the superimpose of spectral bands is observed in Raman spectra of CTO-KMO composites, related to each individual phase, verifying the presence of CTO and KMO in ceramic composites (Fig. ab) but with no interdiffusion. Moreover, the intensities of KMO Raman modes are found to increase gradually with increase in KMO concentration.

Back-scattered electron (BSE) images of polished surfaces for cold-sintered CTO-xKMO are shown in Fig. 2(a-c). Microstructures appear dense in all studied ceramic composites (also observed in fracture surface of CTO-BMO, Fig. 2d), in agreement with data given in Table I. Image contrast indicates that the microstructure is composed of two chemically discrete and distinct phases which are identified by EDS mapping (Fig. 2e-j) as KMO (light contrast) and CTO (dark contrast), respectively, consistent with XRD patterns and Raman spectra (Figure 1). To check the compatibility of CTO-xKMO composite ceramics with Ag electrodes, Ag paste was introduced in the cold-sintered CTO-0.92KMO composite ceramics, with BSE images shown in Fig. 2(k,l). The bright regions correspond to Ag due to its greater weight averaged atomic number than CTO-0.92KMO with no evidence of reaction at the ceramic/electrode interface, indicating good compatibility.

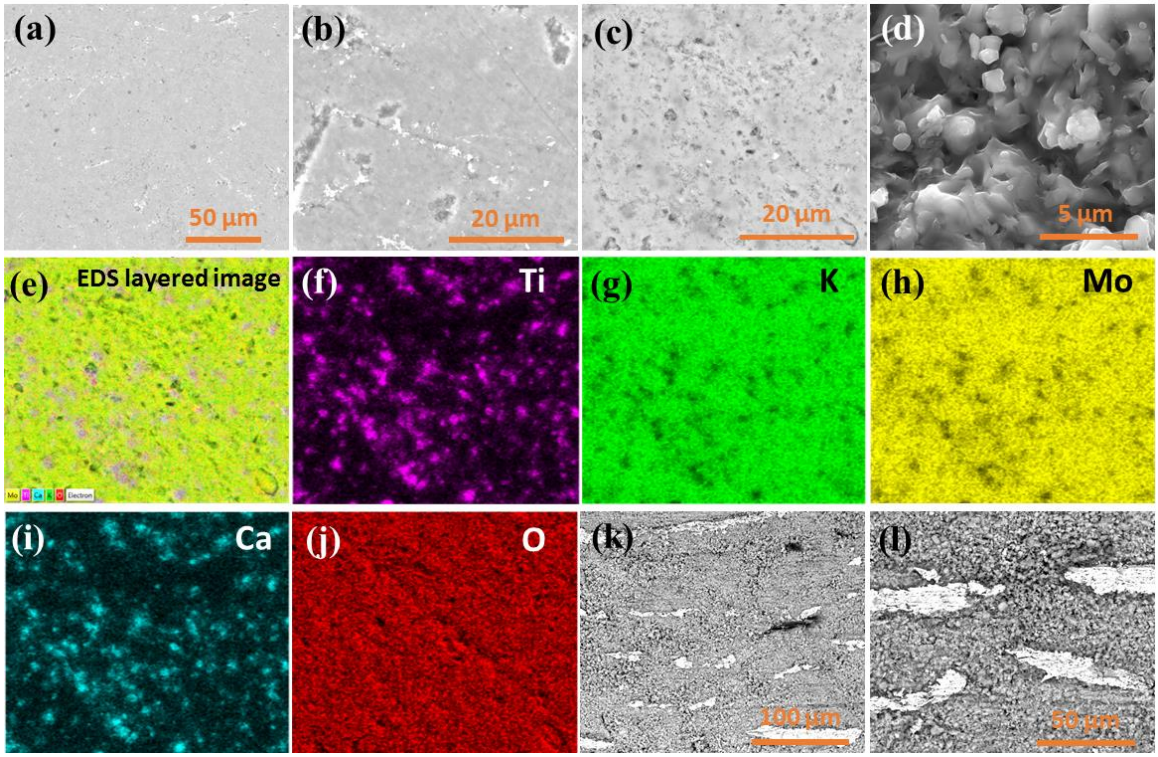

Figure 2. The BSE images of cold-sintered (a) CTO-0.2KMO, (b) CTO-0.5KMO, and (c) CTO-0.92KMO polished surfaces. (d) The SEM image of cold-sintered CTO-20%KMO fracture surface. EDS elemental mapping results of polished CTO-0.92KMO samples: (e) elemental layered image, (f) Ti, (g) K, (h) Mo, (i) Ca, (j) O. (k,l) The BSE images of cold-sintered CTO-0.92KMO with Ag paste.

The microwave dielectric properties of CTO-xKMO composite ceramics as a function of weight fraction (x) KMO are presented in Fig. 3 and listed in Table I. ε_r and TCF decrease linearly from 46.6 and +317 ppm/°C, respectively, for CTO-0.2KMO to 6.4 and -70 ppm/°C for KMO. $Q\times f$ increases from 1000 GHz for CTO-0.2KMO to 26470 GHz for KMO, as shown in Fig. 3 and Table I. A near-zero TCF (-4 ppm/°C) is achieved for CTO-0.92KMO with a low ε_r ~ 8.5 and $Q\times f$ ~ 11,000 GHz. Assuming no chemical interactions between the respective phases, the effective ε_r of composites may be predicted by mixing laws (Equations 4-6).[31-32]

series law, $1/\varepsilon = V_1/\varepsilon_1 + V_2/\varepsilon_2$ (4)

parallel law, $\varepsilon = V_1 \times \varepsilon_1 + V_2 \times \varepsilon_2$ (5)

logarithmic law, $\varepsilon = \varepsilon_1^{V_1} \varepsilon_2^{V_2}$ i.e. $\lg\varepsilon = V_1 \lg\varepsilon_1 + V_2 \lg\varepsilon_2$ (6)

where ε_1 and V_1 is the ε_r and volume fraction (V) of phase 1, ε_2 and V_2 is the ε_r and V of phase 2 ($V_1 + V_2 = 1$). In Fig. 3, ε_r of CTO-KMO is close to the values calculated using Equation (6), following a logarithmic mixing law with the respective weight fraction. TCF and $Q \times f$ of composites can be predicted by using a parallel and series mixing rule, respectively

$TCF = V_1 \times TCF_1 + V_2 \times TCF_2$ (7)

$1/(Q \times f) = V_1/(Q_1 \times f_1) + V_2/(Q_2 \times f_2)$ (8)

where TCF_1, $Q_1 \times f_1$ and TCF_2, $Q_2 \times f_2$ correspond to the TCF and $Q \times f$ values of phase 1 and phase 2, respectively, Fig. 3(b).

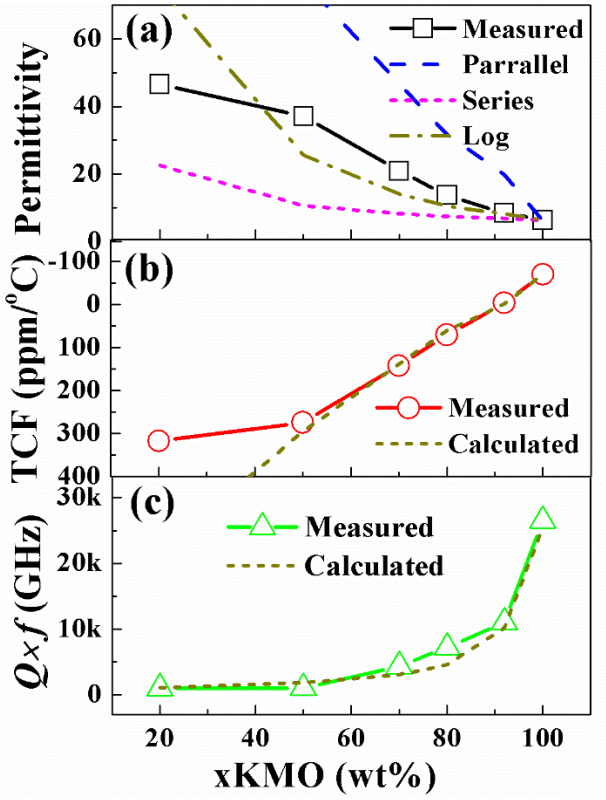

Figure 3. The microwave dielectric properties (a) ε_r, (b) TCF and (c) $Q \times f$ of CTO-xKMO composite ceramics as a function of x (KMO fraction).

Microstrip patch antennas are common RF components that have the advantages of low cost, low profile and easy fabrication, which makes them popular for consumer wireless devices such as mobile phones and tablets. A microstrip patch antenna consists of a top radiation element and a bottom ground plane, separated by a dielectric substrate. The dielectric substrate plays an important role to optimise antenna performance such as bandwidth and antenna efficiency.

A rectangular microstrip patch antenna was fabricated from 40.0 mm × 40.0 mm × 1.4 mm CTO-0.92KMO substrate prepared by cold sintering. The radiation element and ground plane were made from copper tape with a thickness of ~0.05 mm. The radiation element had the dimension of 27.5 mm × 23.0 mm, while the ground plane has the same dimension as the substrate. A coaxial probe feed was used with a feed point ~6 mm from the long edge (27.5 mm edge) of the radiation element. The described dimension resulted in a microstrip patch antenna operating at a resonant frequency of ~2.5 GHz. An image of the fabricated microstrip patch antenna is shown in the inset of Figure 4(a). The measured s11 result of the antenna is shown in Figure 4(a). It shows the impedance of the antenna is well matched with s11 = -14.2 dB at 2.51 GHz. The measured radiation pattern on the E-plane (the electric field vector) and the H-plane (the magnetic field vector, normal to the electric plane) of the antenna are shown in Figure 4(b). The realised gain of this antenna at 2.5 GHz was 2.73 dB, which led to a radiation efficiency of 62.0%. The low sintering temperature of the ceramic (150 ^{o}C) and the excellent antenna performance confirm the potential of directly fabricating antenna substrates onto metallised PCBs for future integrated 5G antenna applications.

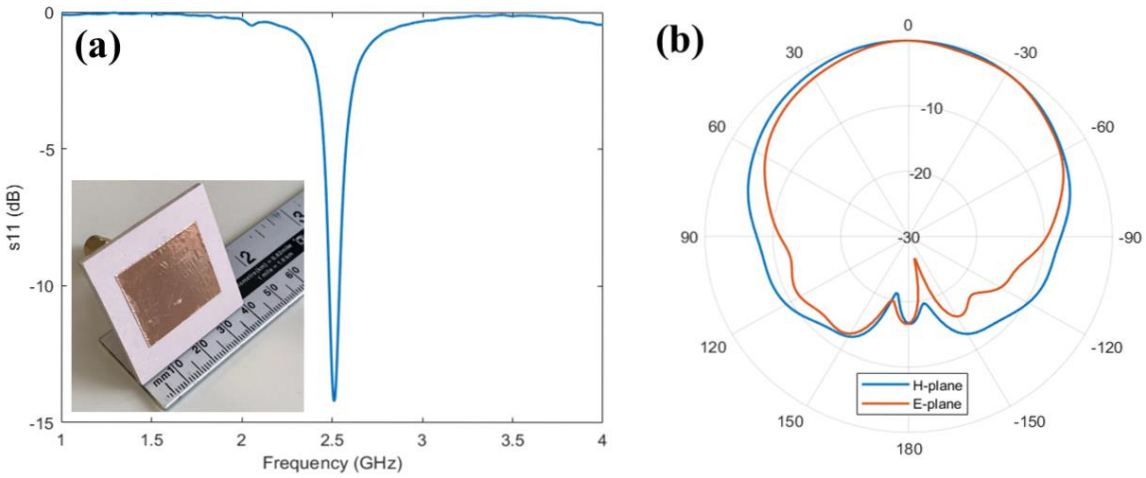

Figure 4. Measured (a) s11, and (b) radiation pattern of the CTO-0.92KMO microstrip antenna. The picture of fabricated microstrip antenna is given in the inset of (a).

CONCLUSIONS

Cold sintered CTO-KMO microwave composite ceramics with 89%-100% relative density were fabricated at 150 °C and a uniaxial pressure of 200 MPa for a hold time of 30 min. Only CTO and KMO phases were present in composite ceramics and there was no evidence of chemical reaction between the two phases by XRD, SEM and Raman spectroscopy. Ag paste was introduced in cold-sintered CTO-0.92KMO samples, and BSE images indicated no evidence of reaction at the interface between ceramic and electrode, suggesting good compatibility for the future fabrication of more complex integrated devices. As the weight fraction of KMO increased, ε_r and TCF decreased and $Q \times f$ increased. A near-zero TCF of +4 ppm/°C was obtained in CTO-0.2KMO with $\varepsilon_r \sim 8.5$ and $Q \times f \sim 11{,}000$ GHz. A microstrip patch antenna was designed and fabricated using cold sintered CTO-0.2KMO as a substrate which operated at 2.51 GHz with a radiation efficiency of 62.0%. Cold sintered CTO-KMO is therefore, considered to have great potential for the fabrication of integrated devices, directly fabricated on metallised PCBs for 5G applications.

ACKNOWLEDGMENTS

We acknowledge the Synthesizing 3D Metamaterials for RF, Microwave and THz Applications EPSRC (EP/N010493/1) and Sustainability and Substitution of Functional Materials and Devices EPSRC (EP/L017563/1) for funding and supporting this work.

REFERENCES

1. I.M. Reaney, D. Iddles, J. Am. Ceram. Soc. 89 (2006) 2063-2072.
2. T. Fujii, A. Ando, Y. Sakabe, J. Eur. Ceram. Soc., 26 (2006) 1857-1860.
3. H. Ohsato, T. Tsunooka, A. Kan, Y. Ohishi, Y. Miyauchi, Key Eng. Mater. 269 (2004) 195-198.
4. M. A. M. Albreem, 5G Wireless Communication Systems: Vision and Challenges, 2015 IEEE International conference on computer, communication, and control technology, Sarala, Malaysia.
5. M. A. Matin, Adv. Electromag. 5 (2016) 98-105.
6. D. Zhou, L. Pang, D. Wang, Z. Q, I.M. Reaney, *ACS Sustain. Chem. Eng.* 6(2018) 11138-11143.
7. L. Pang, D. Zhou, D. Wang, J. Zhao, W. Liu, Z. Yue, I.M. Reaney, J. Am. Ceram. Soc. 101 (2018) 1806-1810.
8. D. Zhou, J. Li, L. Pang, D. Wang, I.M. Reaney, J. Mater. Chem. C 5 (2017) 6086-6091.
9. D. Zhou, J. Li, L. Pang, G.H. Chen, Z.M. Qi, D. Wang, I.M. Reaney, ACS Omega 1 (2016) 963-970.
10. K. Song, P. Liu, H. Lin, W. Su, J. Jiang, S. Wu, J. Wu, Z. Ying, H. Qin, J. Eur. Ceram. Soc. 36 (2016) 1167-1175.
11. J. Song, K. Song, J. Wei, H. Lin, J. Wu, J. Xu, W. Su, Z. Cheng, J. Am. Ceram. Soc. 101 (2018) 244-251.

12. X. Song, K. Du, X. Zhang, J. Li, W. Lu, X. Wang, W. Lei, J. Alloys Comp. 750 (2018)996-1002.
13. L. Li, C. H. Liu, J. Y. Zhu, X. M. Chen, J. Eur. Ceram. Soc. 35 (2015)1799-1805.
14. D. Zhou, C.A. Randall, L. Pang, H. Wang, J. Guo, G. Zhang, X. Wu, L. Shui, X. Yao, J. Am. Ceram. Soc. 94 (2011) 348-50.
15. H. Kahari, M. Teirikangas, J. Juuti, H.Jantunen, J. Am. Ceram. Soc. 97 (2014) 3378-3379.
16. H. Kähäri, M. Teirikangas, J. Juuti, H. Jantunen, Ceram. Inter. 42 (2016) 11442-11446.
17. M. Väätäjä, H, Kähäri, J. Juuti, H. Jantunen, J. Am. Ceram. Soc. 100 (2017) 3626-3635.
18. M. Väätäjä, H, Kähäri, K. Ohenoja, M. Sobocinski, J. Juuti, H. Jantunen, Sci. Rep. 8 (2018) 15955.
19. J. Guo, H. Guo, A.L. Baker, M.T. Lanagan, E.R. Kupp, G.L. Messing, C.A. Randall, Angew. Chem. Int. Ed. 55 (2016) 11457-11461.
20. J. Guo, S.S. Berbano, H. Guo, A.L. Baker, M.T. Lanagan, C.A. Randall, Adv. Funct. Mater. 26 (2016) 7115-7121.
21. A. Baker, H. Guo, J. Guo, C. Randall, J. Am. Ceram. Soc. 99 (2016) 3202-3204.
22. J. Guo, A.L. Baker, H. Guo, M.T. Lanagan, C.A. Randall, J. Am. Ceram. Soc. 100 (2017) 669-677.
23. J.P. Maria, X. Kang, R.D. Floyd, E.C. Dickey, H. Guo, J. Guo, A. Baker, S. Funihashi, C.A. Randall, J. Mater. Res. 32 (2017) 3205-3218.
24. J. Guo, X. Zhao, T.H.D. Beauvoir, J.H. Seo, S.S. Berbano, A.L. Baker, C. Azina, C.A. Randall, Recent Progress in Applications of the Cold Sintering Process for Ceramic–Polymer Composites, Adv. Funct. Mater. 28 (2018) 1801724.
25. I.J. Induja, M.T. Sebastian, J. Eur. Ceram. Soc. 37 (2017) 2143-2147.
26. W. Hong, L. Li, M. Cao, X.M. Chen, J. Am. Ceram. Soc. 101 (2018) 4038-4043.
27. Y. Liu, P. Liu, C. Hu, Ceram. Inter. 44 (2018) 21047-21052.

28. S.S. Faouri, A. Mostaed, J.S. Dean, D. Wang, D.C. Sinclair, S. Zhang, W.G. Whittow, Y. Vardaxoglou, I.M. Reaney, Acta Mater. 166 (2019) 202-207.
29. D. Zhou, L. Pang, D. Wang, I.M. Reaney, J. Eur. Ceram. Soc. 39 (2019) 2374-2378.
30. T. Ibn-Mohammed, C.A. Randall, K.B. Mustapha, J. Guo, J. Walker, S. Berbano, S.C.L. Koh, D. Wang, D.C. Sinclair, I.M. Reaney, J. Eur. Ceram. Soc. 39 (2019) 5213-5235.
31. D. Wang, D. Zhou, S. Zhang, Y. Vardaxoglou, W.G. Whittow, D. Cadman, I.M. Reaney, ACS Sustain. Chem. Eng. 6 (2018) 2438-2444.
32. D. Wang, S. Zhang, D. Zhou, K. Song, A. Feteira, Y. Vardaxoglou, W. Whittow, D. Cadman, I.M. Reaney, Materials 12 (2019) 1370.
33. D. Wang, D. Zhou, K. Song, A. Feteira, C.A. Randall, I.M. Reaney, Adv. Electron. Mater. 5 (2019) 1900025
34. M.T. Sebastian, Dielectric Materials for Wireless Communication. Elsevier Science Publishers, 2008, 165, 172.
35. T. Hirata, K. Ishioka, M. Kitajima, J. Solid State Chem. 124 (1996) 353-359.
36. U. Balachandran, N.G. Eror, Solid State Commun. 44 (1982) 815-817
37. H. Zhenga, G.D.C. Csete de Gy Örgyfalvaa, R. Quimbya, H. Bagshawa, R. Ubicb, I.M. Reaneya, J. Yarwood, J. Eur. Ceram. Soc. 23 (2003) 2653–2659
38. W. Paraguassu, G.D. Saraiva, S. Guerini, P.T.C. Freire, B.T.O. Abagaro, J. Mendes Filho, J. Solid State Chem. 196 (2012) 197-202.
39. G.D. Saraiva, W. Paraguassu, P.T.C. Freire, M. Maczka, J. Mendes Filho, Vib. Spectrosc. 58 (2012) 87-94.